



# 3D-printed hierarchical pillar array electrodes for high-performance semi-artificial photosynthesis

Xiaolong Chen<sup>1</sup>, Joshua M. Lawrence<sup>2</sup>, Laura T. Wey<sup>2</sup>, Lukas Schertel<sup>1</sup>, Qingshen Jing<sup>3</sup>, Silvia Vignolini<sup>1</sup>, Christopher J. Howe<sup>2</sup>, Sohini Kar-Narayan<sup>3</sup> and Jenny Z. Zhang<sup>1</sup>✉

**The rewiring of photosynthetic biomachineries to electrodes is a forward-looking semi-artificial route for sustainable bio-electricity and fuel generation. Currently, it is unclear how the electrode and biomaterial interface can be designed to meet the complex requirements for high biophotoelectrochemical performance. Here we developed an aerosol jet printing method for generating hierarchical electrode structures using indium tin oxide nanoparticles. We printed libraries of micropillar array electrodes varying in height and submicrometre surface features, and studied the energy/electron transfer processes across the bio-electrode interfaces. When wired to the cyanobacterium *Synechocystis* sp. PCC 6803, micropillar array electrodes with microbranches exhibited favourable biocatalyst loading, light utilization and electron flux output, ultimately almost doubling the photocurrent of state-of-the-art porous structures of the same height. When the micropillars' heights were increased to 600  $\mu\text{m}$ , milestone mediated photocurrent densities of 245  $\mu\text{A cm}^{-2}$  (the closest thus far to theoretical predictions) and external quantum efficiencies of up to 29% could be reached. This study demonstrates how bio-energy from photosynthesis could be more efficiently harnessed in the future and provide new tools for three-dimensional electrode design.**

Biocatalysts (from enzymes to living microorganisms) can be electrochemically connected (wired) to electrodes for biotechnological applications or fundamental studies<sup>1–4</sup>. In particular, cyanobacteria (photosynthetic bacteria) are free-living, self-repairing, abundant, solar-powered biocatalysts that can be wired to electrodes for electricity generation (biophotovoltaics; Fig. 1a,b) and chemical synthesis<sup>2,5–7</sup>.

At present, semi-artificial approaches for solar energy conversion are in the nascent phase, and photocurrent densities achievable by cyanobacterial electrodes have been calculated to be between 340  $\mu\text{A cm}^{-2}$  and 2,400  $\mu\text{A cm}^{-2}$  (at the lower estimate, the energy conversion efficiency compares favourably to that of industrial bio-fuel production)<sup>8</sup>. However, typical photocurrents generated by cyanobacterial electrodes are two orders of magnitude below this value. This is despite substantial bioengineering efforts<sup>9,10</sup> to increase biological electron output and the deployment of artificial electron mediators, which can be introduced to maximize electron collection from the photosynthetic electron transport chain (Fig. 1b)<sup>6,8</sup>. The bottleneck in current output probably lies with the electrode itself.

In photoelectrochemical reactions, the electrode structure must balance several factors to minimize reaction bottlenecks<sup>11</sup>. Where biocatalysts are employed, it must compensate for the larger catalyst dimensions and lower overall loading<sup>2,6,12</sup>. The state-of-the-art electrode architecture in both protein film and biofilm photoelectrochemistry is the inverse opal (IO) porous structure<sup>13</sup>, which has been fabricated from a variety of metal oxides<sup>12,14–17</sup>. In particular, indium tin oxide (ITO) exhibits appropriate inertness, conductivity, light scattering and biocompatibility properties<sup>12</sup>. It was demonstrated that the combination of the macroporous structures (offering a large electroactive surface area and aiding biocatalyst penetration) with a meso substructure (aiding biocatalyst adhesion)<sup>7,18</sup> in a hierarchical architecture was important for efficient biocatalyst wiring<sup>19</sup>. When cells of the model cyanobacterium, *Synechocystis* sp. PCC 6803 (*Synechocystis*), were immobilized onto IO-ITO electrodes, a

mediated photocurrent density of 14  $\mu\text{A cm}^{-2}$  (Fig. 1c) and external quantum efficiency (EQE) of 2.7% were observed<sup>7</sup>. It is uncertain where the bottleneck in photocurrent lies (Supplementary Note 1). Further progress in electrode design has been limited by the lack of versatile fabrication techniques that can generate large libraries of hierarchical electrode structures.

Here we developed an aerosol jet printing method for the efficient and reproducible fabrication of large libraries of micropillar electrodes made from ITO nanoparticles. We demonstrated that this printing method could produce tuneable hierarchical features spanning five orders of magnitude in length scales in one printing step. This enabled us to fabricate libraries of hierarchical micropillar array electrodes (Supplementary Note 1)<sup>20,21</sup> using ITO nanoparticles (Fig. 1d–f), which is not possible using other fabrication methods. We varied the heights and surface roughness of the pillars to tune the electroactive surface areas on multiple length scales and compared their properties against state-of-the-art IO-ITO electrodes. Using this approach, we expanded current understanding of electrode structure–activity relationships and arrived at a new generation of high-performing photosynthetic electrodes (Fig. 1c).

## Aerosol jet-printed ITO electrodes

Aerosol jet printing is an additive manufacturing technique that can print metal nanoparticle inks (Fig. 2a) with high design flexibility, resolution and material deposition precision<sup>22–26</sup> via a contactless direct write approach<sup>27–30</sup>. However, the fabrication of three-dimensional (3D) hierarchical structures using this technique has not been reported. To establish an aerosol jet printing method for the fabrication of 3D structures using an ITO nanoparticle ink, considerable deviations from classical ink compositions and printing parameters were needed (Fig. 2; see Supplementary Note 2 for a tutorial explanation of aerosol jet printing).

To produce pillar structures, a new parameter, the gas focusing pressure ratio, which is the balance between the pressure of the

<sup>1</sup>Yusuf Hamied Department of Chemistry, University of Cambridge, Cambridge, UK. <sup>2</sup>Department of Biochemistry, University of Cambridge, Cambridge, UK. <sup>3</sup>Department of Materials Science and Metallurgy, University of Cambridge, Cambridge, UK. ✉e-mail: [jz366@cam.ac.uk](mailto:jz366@cam.ac.uk)

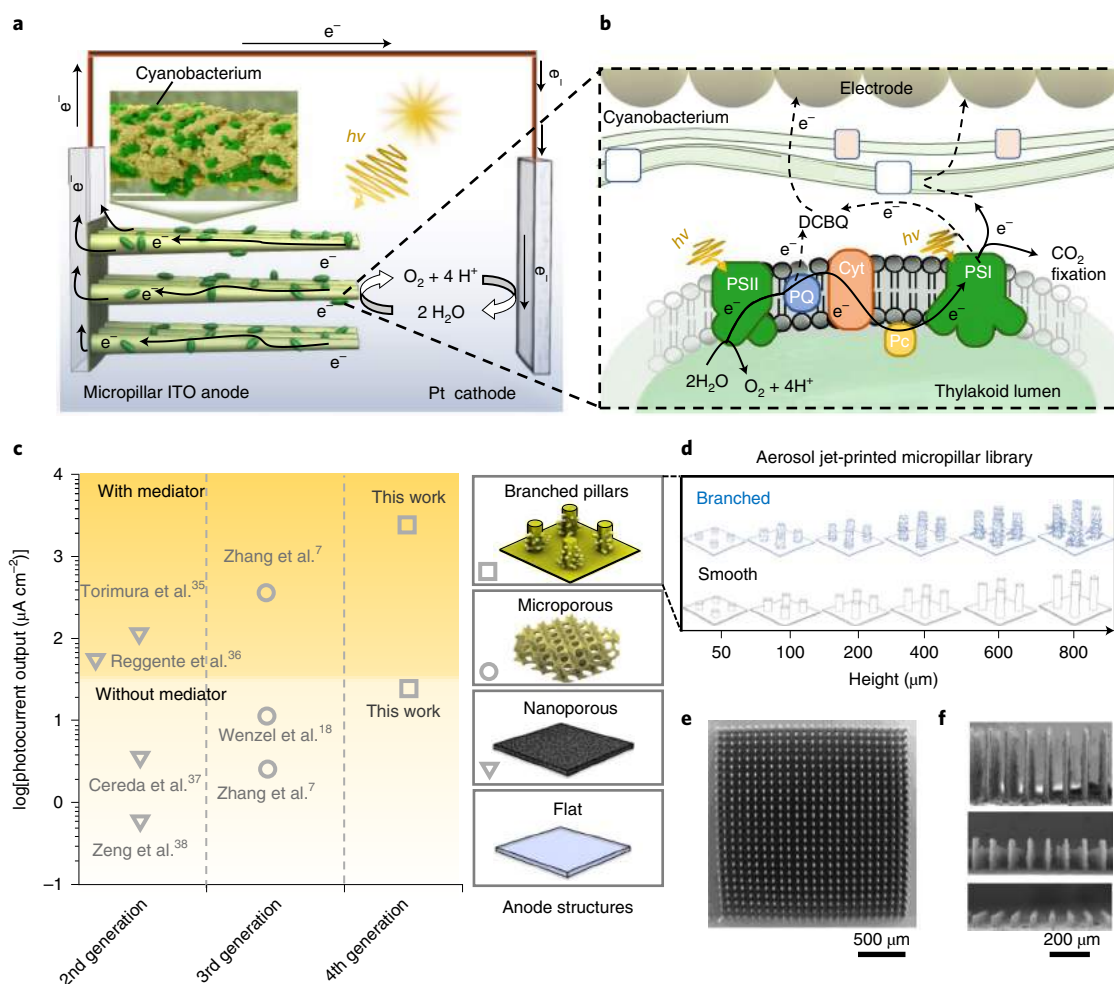


**Fig. 1 | Next-generation electrodes for biophotocatalysis.** **a**, Schematic of a biophotocatalytic cell performing biological solar electricity generation using photosynthetic biofilms as photocatalysts. Electron flux originating from photosynthetic water oxidation is collected at the anode and transferred to a cathode, which reduces oxygen back to  $\text{H}_2\text{O}$ . Inset: colorized SEM image of a micropillar with cyanobacteria-adsorbed electrode printed from ITO nanoparticles. Scale bar, 10  $\mu\text{m}$ . **b**, Schematic of the cyanobacterium–anode interface. Light is collected by photosystem II (PSII), which is used to oxidize water, resulting in the liberation of electrons,  $\text{O}_2$  and  $\text{H}^+$ . The electrons are transferred through the photosynthetic electron transport chain to photosystem I (PSI), which pumps absorbed light energy into the electrons. The electrons can be used in a range of reductive pathways in the cell, including the Calvin–Benson cycle for  $\text{CO}_2$  fixation. Some electrons from photosynthesis undergo extracellular electron transport, which can be enhanced by exogenous electron mediators, such as DCBQ, shuttling electrons to the electrode<sup>6</sup>. **c**, Photocurrent output from select key cyanobacterial electrodes corresponding to different generations of electrode design<sup>7,18,35–38</sup>. **d**, The library of aerosol jet-printed micropillar ITO electrodes presented in this study. **e**, SEM image of a printed micropillar array electrode (top view). **f**, SEM images of printed micropillar array electrodes (20  $\mu\text{m}$  diameter, 100  $\mu\text{m}$  spacing) of different heights (side view).

carrier gas and the sheath gas, was tuned (Fig. 2b). It was observed that at ratios of between 2.4 and 3.5, pillars of up to 800  $\mu\text{m}$  could be printed. Below this range, insufficient materials would be deposited; above this range, an ‘overspill’ effect occurred, resulting in a thick unstable pillar base (Fig. 2b, inset).

We endowed the printed pillars with micro-scale roughness by changing to non-classical cosolvent systems, such as water (non-volatile) and methanol (MeOH, volatile), in the ink precursor. The ratio of the water to methanol was varied to result in aerosol streams of different droplet sizes and volatilities (Supplementary Table 1): high water content (>50% v/v) gave rise to ‘droplet-like’ features (Supplementary Fig. 1a); a methanol content of 50–65% v/v gave rise to ‘smooth’ nanoporous pillars (Fig. 2d and Supplementary Fig. 1b); a methanol content of 65–75% v/v gave rise to submicrometre-sized branched features (Fig. 2e); and at a methanol content of >75% v/v, the diameter of the pillar became thin and brittle

(Supplementary Fig. 1c). The microbranches formed during the printing of the pillars were attributed to formation of smaller aerosol droplets at higher methanol contents. The small droplets near the sheath gas interface were too small to resist the turbulence at the side of the deposited area and were further broken up at the turbulent front. The submicrometre droplets formed follow wide trajectory patterns, to result in the branched features, with the volatility of the cosolvent mixture aiding rapid solidification of the structure.

We identified ideal conditions for generating arrays of well-formed smooth micropillars of ITO nanoparticles (SP-ITO; Fig. 2d) and branched micropillars of ITO nanoparticles (BP-ITO, Fig. 2e), and electrodes varying in pillar height (50–800  $\mu\text{m}$ ) and roughness were printed for this study (Fig. 1d and Supplementary Fig. 2). The conditions used for the printing of the micropillar electrodes (20  $\mu\text{m}$  diameter, 50–800  $\mu\text{m}$  height, 100  $\mu\text{m}$  centre-to-centre spacing) are documented in Supplementary Table 2.

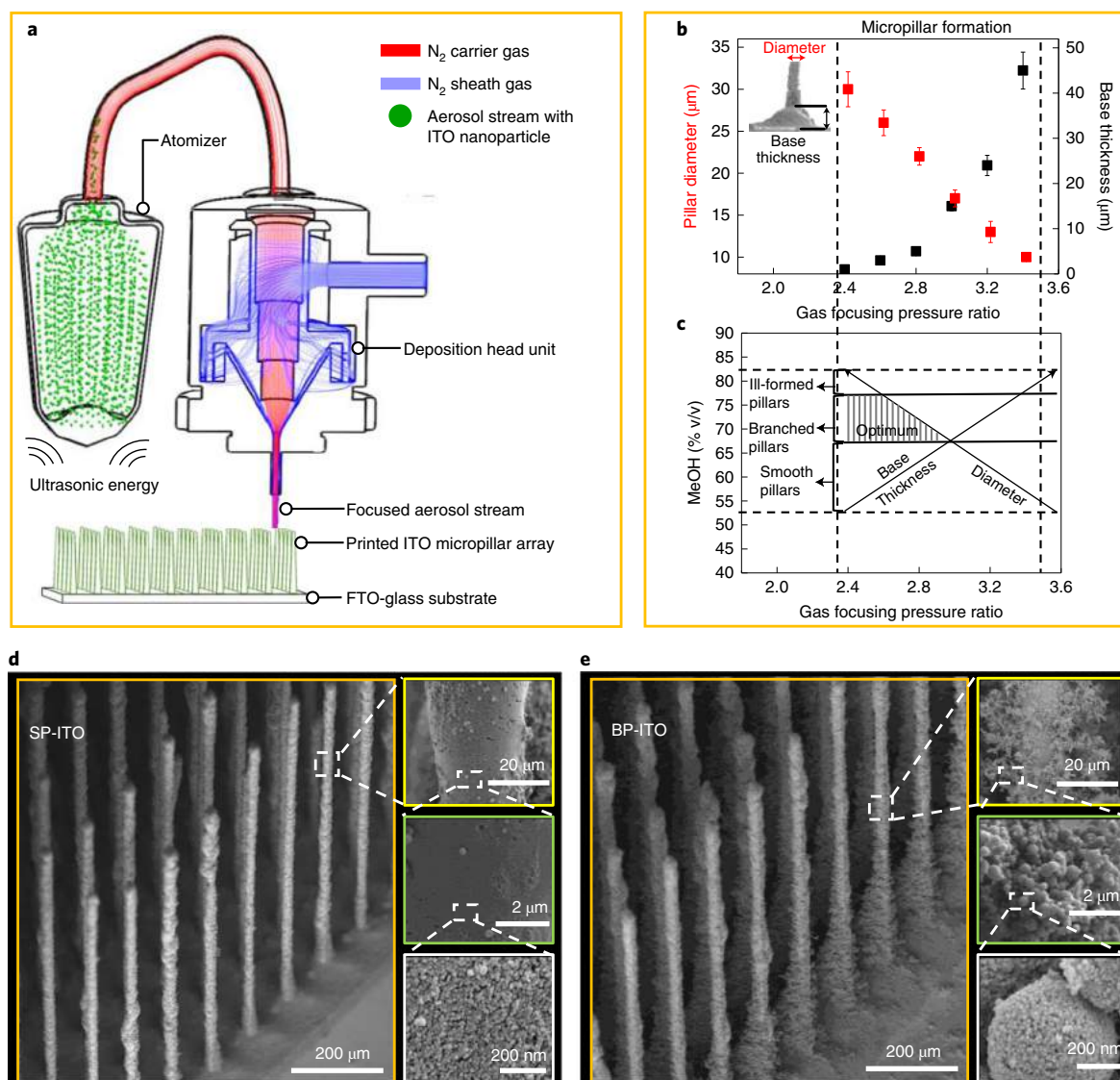


**Fig. 2 | Aerosol jet printing of micropillar array electrodes.** **a**, Schematic of the printing process. The ITO nanoparticle in methanol/water ink precursor was placed in an ultrasonic atomizer where it was aerosolized, entrained in an  $N_2$  carrier gas stream and aerodynamically focused via a stream of coaxial  $N_2$  sheath gas. The micropillar ITO structures were printed onto an FTO-coated glass. **b**, Printing parameters for producing micropillars. The gas focusing pressure ratio was identified as a key control parameter for tuning pillar shape. Inset: SEM image of a representative printed pillar with a base. **c**, Printing parameters for producing submicrometre roughness. An optimal operational window between gas focusing pressure ratio and ink MeOH content was identified to form microdroplet branches. **d**, SEM image of a representative smooth micropillar ITO (SP-ITO) electrode with a height of 600  $\mu\text{m}$  and diameter of 20  $\mu\text{m}$ . Images obtained at higher magnifications show nano features resulting from the packing of the nanoparticles. The SP-ITO was fabricated using a focusing pressure ratio of 2.5 and MeOH volume fraction of 60%. **e**, SEM image of a representative branched micropillar ITO (BP-ITO) electrode with a height of 600  $\mu\text{m}$  and diameter of 20  $\mu\text{m}$ . Images obtained at higher magnifications show microbranch features comprising submicrometre droplets. Further magnification of the droplet features shows nano features of the nanoparticles. The BP-ITO was fabricated using a gas focusing pressure ratio of 2.5 and MeOH volume fraction of 70%. Error bars represent the standard error of the mean ( $n=3$ ).

### Characterization of the printed micropillar electrodes

The printed micropillar electrodes were annealed and confirmed to retain the ITO composition via energy-dispersive X-ray spectroscopy (EDX; Supplementary Fig. 3). Scanning electron microscopy (SEM) images of the libraries of the annealed SP-ITO and BP-ITO structures showed that the printed pillars within each array were uniform in height and diameter. We observed that the branching decreased with the height of the BP-ITO structure, with reduced branching at the top half of pillars at heights  $>400\mu\text{m}$  (Supplementary Fig. 2). This was attributed to the decrease in turbulence during the printing process, as the distance between the printer nozzle and the tip of the pillar decreased.

The optical properties of the printed micropillar bare electrodes (in air) were measured with the aid of an integrating sphere (Supplementary Figs. 4–6) and compared against benchmark third-generation IO-ITO electrodes (10  $\mu\text{m}$  in pore size, 50  $\mu\text{m}$  in height; Supplementary Fig. 7) and are shown in Fig. 3a–d. We observed that when irradiated with  $0^\circ$  vertical incident white light ( $1\text{mWcm}^{-2}$ ), the bare IO-ITO structure transmitted  $4.4\pm2.0\%$  and reflected  $12.4\pm1.6\%$  of the incident light; the SP-ITO array structure of the same height transmitted  $32.5\pm0.7\%$  and reflected  $15.6\pm1.0\%$  of the incident light, whereas the BP-ITO array structure transmitted  $26.4\pm2.1\%$  and reflected  $20.2\pm2.2\%$  of the incident light (Fig. 3c). As such, micropillar structures exhibited significantly



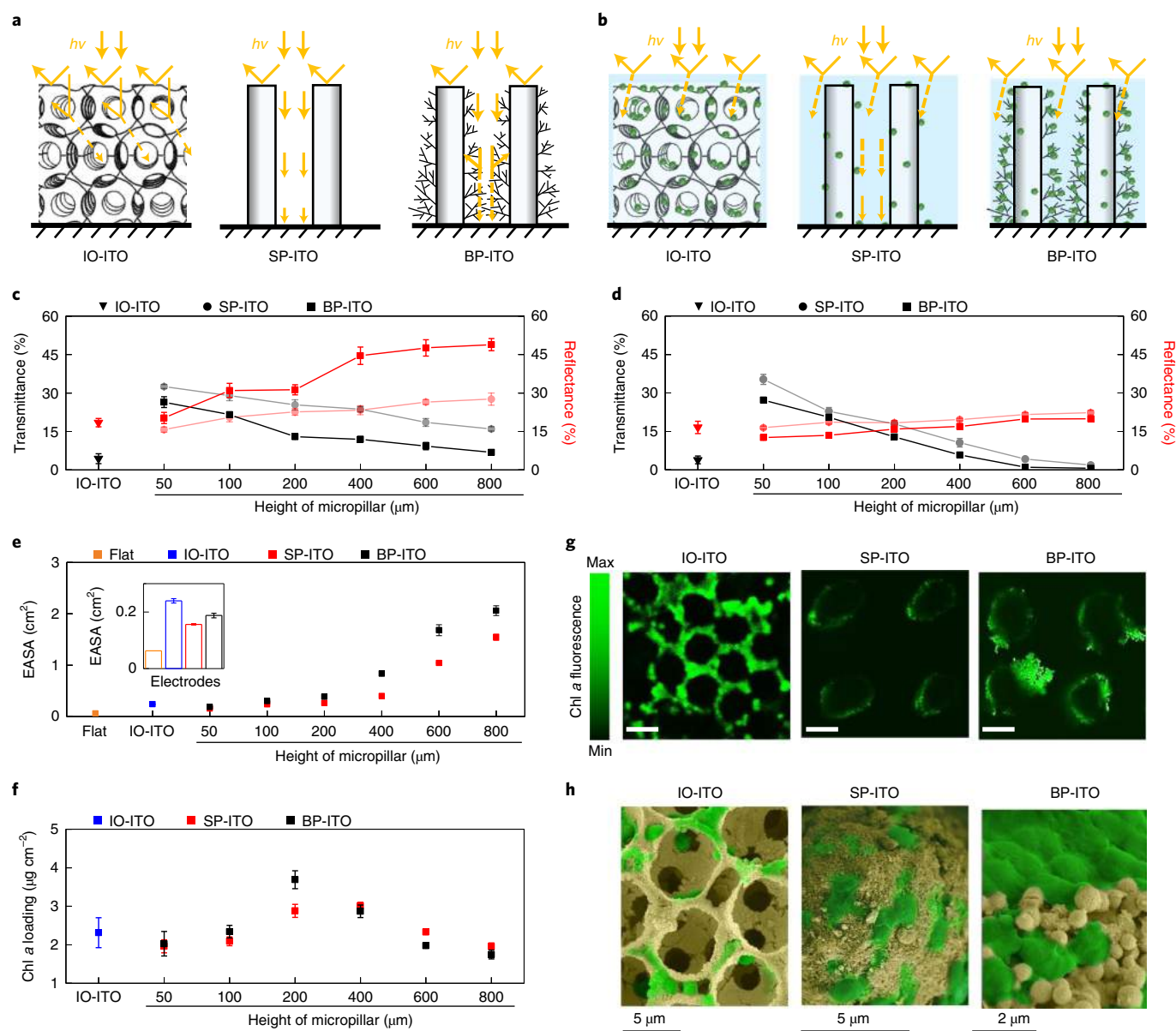


**Fig. 3 | Printed micropillar electrodes exhibit high light transmission and cell loading.** **a**, Schematic of bare electrodes interacting with light. **b**, Schematic of electrodes with immobilized cells interacting with light. **c**, Light transmittance and reflectance studies of bare electrodes in air. **d**, Light transmittance and reflectance studies of electrodes incubated with cells. Light transmittance and reflectance studies were carried out using  $0^\circ$  vertical incident white light ( $1 \text{ mW cm}^{-2}$ ). The IO-ITO electrodes were  $50 \mu\text{m}$  in height, the SP-ITO and BP-ITO electrodes ranged from  $50 \mu\text{m}$  to  $800 \mu\text{m}$  in height. Concentrated suspensions of *Synechocystis* cells ( $150 \text{ nmol (Chl } a) \text{ ml}^{-1}$  in BG11 medium) were incubated with electrodes for 12 h, the electrodes were gently washed with the fresh medium before measurements. **e**, EASA of flat, IO-ITO, SP-ITO and BP-ITO electrodes determined via capacitance measurements. Inset: zoomed-in comparison of the EASA of flat, IO-ITO, SP-ITO and BP-ITO electrodes all of  $50 \mu\text{m}$  height. **f**, EASA-normalized Chl *a* loading on electrodes following 12 h incubation with *Synechocystis* and a gentle medium wash. **g**, Representative confocal microscopy images showing a cross-section through the middle of *Synechocystis*-loaded electrodes. Scale bar,  $20 \mu\text{m}$ . **h**, Representative colourized SEM images of *Synechocystis*-loaded electrodes (top view). Error bars represent the standard error of the mean ( $n=3$ ).

enhanced light transmission ( $P \leq 1.6 \times 10^{-3}$ ) compared to IO-ITO, with BP-ITO also exhibiting enhanced scattering ( $P = 3.2 \times 10^{-2}$ ). From this, it could be predicted that much greater light collection by the *Synechocystis*-loaded electrodes is possible with the micropillar microbranched structures. The remainder of the incident light could be attributed to light absorbance by the material or loss from in-plane scattering. This was much higher for the IO-ITO structure ( $83.2 \pm 2.6\%$ ) than for the SP-ITO ( $51.9 \pm 0.3\%$ ) and BP-ITO structures ( $53.3 \pm 3.8\%$ ,  $P \leq 2.5 \times 10^{-3}$ ) (Supplementary Fig. 8).

SP-ITO and BP-ITO electrodes ranging from  $50 \mu\text{m}$  to  $800 \mu\text{m}$  in height (such heights were not accessible for IO-ITO) were also characterized. The transmittance of the bare SP-ITO and BP-ITO electrodes linearly decreased with the increase in height, which was partially due to the corresponding increase in thickness of the pillar base. The overall transmittance of SP-ITO was higher than that of BP-ITO because the microbranches blocked approximately 8% of the incident light; similarly, the reflectance of BP-ITO was enhanced due to the increased scattering arising from the branch-like

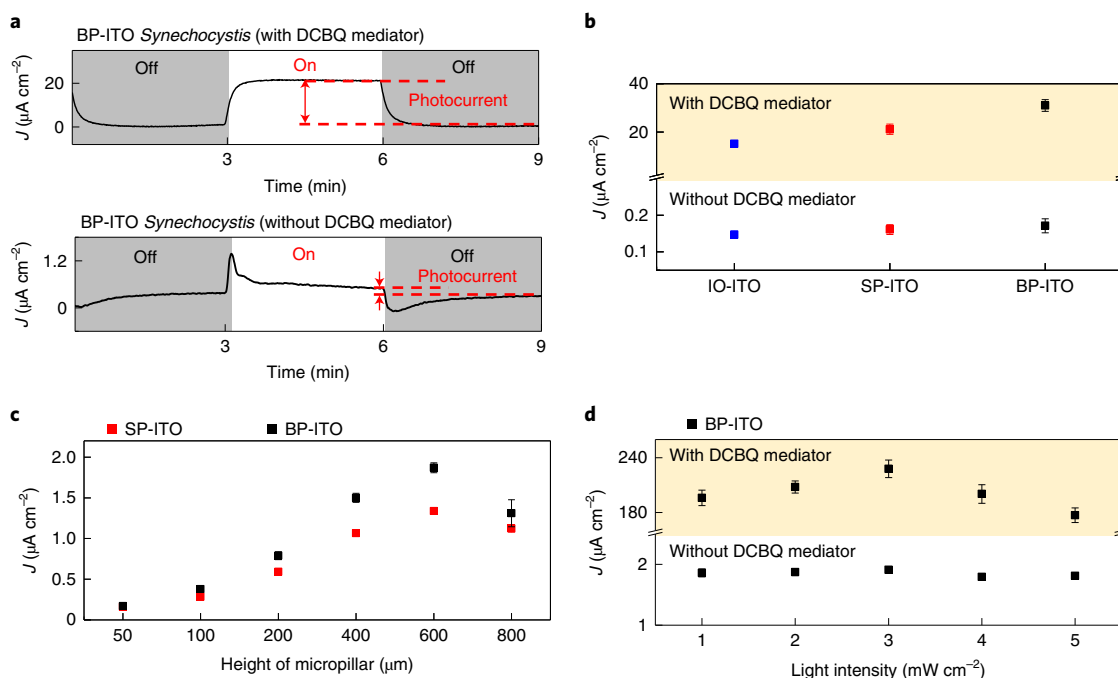


**Fig. 4 | The photoelectrochemical performance of the *Synechocystis*-loaded electrodes.** **a**, Representative photocurrent profile obtained from a *Synechocystis*-loaded BP-ITO electrode in the presence and absence of the exogenous electron shuttle DCBQ (1 mM). **b**, Summary of mediated and non-mediated photoelectrochemical performances of *Synechocystis*-loaded electrodes with different electrode architecture at equivalent thickness (50  $\mu\text{m}$ ) under red light (680 nm, 1  $\text{mW cm}^{-2}$ ). **c**, Summary of non-mediated photoelectrochemical performances of the *Synechocystis*-loaded SP-ITO and BP-ITO electrodes with varying pillar heights without exogenous electron shuttles under red light (680 nm, 1  $\text{mW cm}^{-2}$ ). **d**, The photoelectrochemical performance of optimized *Synechocystis*-loaded BP-ITO electrodes (600  $\mu\text{m}$  pillar height) under white light conditions of different intensities. Chronoamperometry experiments were performed with an applied potential of 0.3 V and 0.5 V versus SHE in the absence and presence of DCBQ, respectively, and in BG11 (pH 8.5) at 25  $^{\circ}\text{C}$ . Error bars represent the standard error of the mean ( $n = 3$ ).

feature<sup>31</sup>. The reflectance was proportional to the height of the bare pillar structures (Fig. 3c).

The electrodes were incubated with a concentrated culture of *Synechocystis* (~1.4  $\mu\text{m}$  in diameter) for 12 h in the dark, gently rinsed, then immersed in aqueous BG11 medium for transmittance and reflectance measurements. Slight decreases in transmission and reflectance were observed for the *Synechocystis*-loaded IO-ITO electrodes (Fig. 3d), which correspond to a very small change in absorbance (<5%; Supplementary Fig. 8a). However, in the presence of the adhered *Synechocystis* there was a significant decrease in the transmittance ( $P \leq 3.7 \times 10^{-4}$ ) and reflectance ( $P \leq 4.7 \times 10^{-3}$ ) of the taller (600  $\mu\text{m}$ ) micropillar electrodes (Fig. 3d). The presence of cells on the electrodes increased light absorption by up to 40% for the tallest pillar structures (Supplementary Fig. 8b). This could be attributed to light absorption by chlorophyll *a* (Chl *a*) and other pigments<sup>32</sup>, which absorb light to drive photosynthesis.

The electroactive surface areas (EASAs) of the bare electrode structures were measured using capacitance measurements (Fig. 3e and Supplementary Fig. 9). When structures of the same height (50  $\mu\text{m}$ ) and geometric area (0.0625  $\text{cm}^2$ ) were compared, IO-ITO had the highest EASA ( $0.24 \pm 0.01 \text{ cm}^2$ ), followed by BP-ITO ( $0.19 \pm 0.01 \text{ cm}^2$ ), then SP-ITO ( $0.160 \pm 0.003 \text{ cm}^2$ ). The deviation of the measured EASA from the theoretical EASA (Supplementary Fig. 9b) in the case of IO-ITO is expected. Although regions of orderly IO structures dominated, the electrode structure contained cracks (Supplementary Fig. 7) and regions of heterogeneity, which may be inaccessible to the electrolyte. In contrast, the theoretical EASAs of the micropillar electrodes matched almost exactly with the experimentally measured values, which indicated that the electrolyte reached the entire printed structure and most of the ITO structure was electrochemically connected.

The cell-loading capacity of each electrode structure was measured spectroscopically by assaying the Chl *a* content on the electrodes, following the experiments. With increasing pillar heights, higher total Chl *a* loading normalized by geometric area could be observed (Supplementary Fig. 10); however, the relationship was not linear and Fig. 3f shows the Chl *a* loading density normalized by the electrode EASA. The micropillar electrodes exhibited comparable normalized cell loadings to IO-ITO at pillar heights of 50 and 100  $\mu\text{m}$ , with the BP-ITO structure at pillar height of 200  $\mu\text{m}$  exhibiting the highest EASA-normalized cell density ( $3.69 \pm 0.23 \mu\text{g cm}^{-2}$ ), which was 60% higher in absorbed Chl *a* content compared to the IO-ITO electrode. The normalized Chl *a* content for the micropillar electrodes declined at heights above 200  $\mu\text{m}$ , which is attributed to the decrease in microbranching in the case of the BP-ITO and gravitational effects (cells settling on the base) limiting cell attachment at the pillar tops. Following cell immobilization, the structures of the printed electrodes were observed to be unchanged (Supplementary Figs. 11 and 12).

Confocal fluorescence microscopy was employed to acquire Z-stacks of the cell-loaded electrodes, exploiting the intrinsic fluorescence of Chl *a* (Fig. 3g and Supplementary Fig. 13). *Synechocystis* cells were distributed non-uniformly throughout IO-ITO, with the greatest cell density being observed near the top of the electrode. *Synechocystis* cells were distributed uniformly along the pillars of the SP-ITO, with a greater density of cells depositing on the base of the pillars. *Synechocystis* cells were also distributed uniformly along the pillars of the BP-ITO, with a higher density of cells observed on the branches of the pillars. Enlarged colorized SEM images showed the distribution of cells from the top view of the electrodes (Fig. 3h). The cells were more densely distributed on the SP-ITO compared to IO-ITO, but most densely distributed on the BP-ITO, forming patches of biofilms.

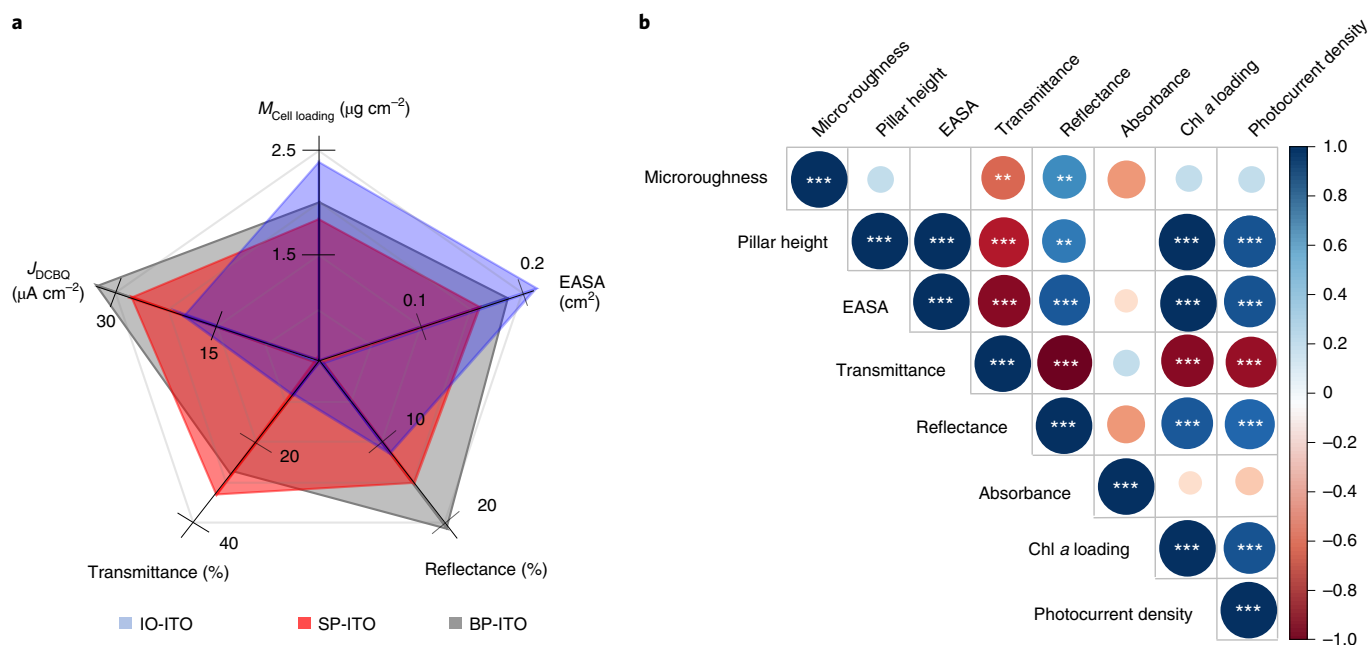


**Fig. 5 | Structure-activity relationship analysis. a**, Radar chart comparison between IO-ITO, SP-ITO and BP-ITO electrode structures (50  $\mu m$  in height).  $J_{DCBO}$ , DCBQ mediated photocurrent density;  $M_{Cell loading}$ , cell loading inferred from Chl *a* content. **b**, Spearman's rank correlation matrix of micropillar electrodes and their properties. The scale bar represents the strength and sign of the correlation coefficient ( $R$ ), with blue indicating a positive and red a negative correlation coefficient. Asterisks indicate significance where \*  $P \leq 0.1$ ; \*\*  $P \leq 0.05$  and \*\*\*  $P \leq 0.01$ .

### Biophotoelectrochemical output

The overall biophotoelectrochemical output was assessed using chronoamperometry under dark/light cycles with moderate light ( $\lambda_{680nm}$ ,  $1 mW cm^{-2}$ ). A three-electrode configuration was employed with the *Synechocystis*-loaded electrode as the working electrode.

In the absence of an exogenous electron mediator, *Synechocystis*-loaded micropillar ITO electrodes produced a characteristic photocurrent profile of *Synechocystis* biofilms (Fig. 4a and Supplementary Fig. 14)<sup>7</sup>, the features of which are still under investigation<sup>33</sup>. The addition of the commonly used membrane-permeable electron mediator 2,6-dichloro-1,4-benzoquinone (DCBQ) resulted in approximately 80-fold, 100-fold and 110-fold increases for the IO-ITO, SP-ITO and BP-ITO electrodes (Fig. 4b), respectively, compared to their corresponding unmediated photocurrents. The effect of the mediator was greater for the micropillar array electrodes, which indicated that many cells on the electrode scaffold were not directly wired. This could be attributed to the multi-layer of cells on the base of the electrode (Supplementary Fig. 11c) or loosely attached cells on the periphery of the microbranches (Supplementary Fig. 11d). The mediated photocurrent densities for *Synechocystis*-loaded BP-ITO electrodes were twice those of IO-ITO electrodes of the same height ( $P = 3.6 \times 10^{-3}$ ) (Fig. 4b).

The non-mediated photocurrent density was also assessed as a function of pillar height for the SP-ITO and BP-ITO electrodes (Fig. 4c and Supplementary Fig. 15). The photocurrent density ( $J$ ) peaked at pillar heights of 600  $\mu m$  (SP,  $1.43 \pm 0.04 \mu A cm^{-2}$ ; BP,  $1.87 \pm 0.06 \mu A cm^{-2}$ ;  $P \leq 2.0 \times 10^{-3}$ ), with a drop observed for electrodes with 800  $\mu m$  pillars. The drop was attributed to the mechanical instability at 800  $\mu m$ , which may be the height limit of pillars printable by the aerosol jet printing method.

In this comparison study, *Synechocystis*-loaded BP-ITO electrodes at 600  $\mu m$  pillar height produced the highest non-mediated photocurrents. In the presence of mediators, EQE measurements carried out using red (680 nm) light at  $1 mW cm^{-2}$  for this electrode showed that  $29 \pm 1\%$  of the light was converted to current ( $158 \pm 5 \mu A cm^{-2}$ ; Supplementary Table 3), which aligned well with the 40% calculated

light absorption by cells immobilized on this electrode (Supplementary Fig. 8b). This is a tenfold higher efficiency than the cell-loaded IO-ITO electrodes under analogous lighting conditions<sup>7</sup>.

To determine the maximum photocurrent output that could be generated using this electrode under more realistic conditions, we changed to a white light source and increased the intensity until maximum photocurrent output was observed at  $3 mW cm^{-2}$ . Under  $3 mW cm^{-2}$  white light, non-mediated photocurrent outputs of  $1.91 \pm 0.03 \mu A cm^{-2}$  and mediated photocurrents of  $236 \pm 10 \mu A cm^{-2}$  were observed (Fig. 4d and Supplementary Table 3). This is an order of magnitude enhancement compared to previous benchmark photosynthetic biofilm systems and is within reach of the calculated theoretical photocurrent densities that could be achieved by living photosynthetic electrodes (lower estimate:  $340 \mu A cm^{-2}$ ). Considering that less than 40% of the incident light was absorbed by the cells (Supplementary Fig. 8), further improvements to the system are still possible via changes to the electrode structure to increase cell loading and light utilization.

### Structure-activity relationships

Two sets of comparisons were carried out: (1) between three different electrode architectures made with the same ITO nanomaterials, height and geometric area; and (2) amongst libraries of micropillar ITO electrodes of different heights and surface roughness.

In the first comparison (Fig. 5a and Supplementary Fig. 14), *Synechocystis*-loaded BP-ITO electrodes (50  $\mu m$  height) yielded twofold higher mediated photocurrent densities than the *Synechocystis*-loaded IO-ITO electrode (50  $\mu m$  height,  $P = 3.6 \times 10^{-3}$ ) despite the IO-ITO structure exhibiting 21% higher EASA ( $P = 1.4 \times 10^{-3}$ ). This implies that light flux into the biophoto-electrode interface was limiting performance of the IO-ITO structure. *Synechocystis*-loaded BP-ITO electrodes resulted in mediated photocurrent densities of  $31 \pm 2 \mu A cm^{-2}$ , which was significantly higher than the  $21 \pm 2 \mu A cm^{-2}$  of SP-ITO electrodes ( $P = 3.9 \times 10^{-2}$ ); this was attributed to the microbranching resulting in significant enhancements to the EASA (23%,  $P = 4.0 \times 10^{-3}$ ).

In the second comparison, a Spearman's rank correlation matrix was calculated from the library of micropillar structures to identify correlations between the properties of these electrodes (Fig. 5b, Supplementary Fig. 16 and Supplementary Note 3). Significant and strong correlation was observed between the pillar height of electrodes and their EASA ( $R=0.96$ ,  $P=6.5\times 10^{-7}$ ), transmittance ( $R=-0.79$ ,  $P=2.16\times 10^{-3}$ ), reflectance ( $R=0.71$ ,  $P=1.01\times 10^{-2}$ ), Chl *a* loading ( $R=0.96$ ,  $P=6.5\times 10^{-7}$ ) and photocurrent density ( $R=0.86$ ,  $P=3.09\times 10^{-4}$ ). This implied that the larger surface of taller pillars provided more sites for cell loading and improved the trapping of light within the structure. No significant correlation was observed between pillar microroughness and the photocurrent density across the library, although significant differences were observed for pillars with heights between 100 and 600  $\mu\text{m}$  (100  $\mu\text{m}$ ,  $P\leq 2.0\times 10^{-2}$ ). This suggested that the macroscale features of micropillar electrodes (in this instance, pillar height) were the most important consideration for boosting photocurrent output. However, significant correlations were observed between microroughness and reflectance ( $R=0.63$ ,  $P=2.89\times 10^{-3}$ ); suggesting that microroughness was important for introducing favourable photonic effects (important for low light conditions).

## Conclusion

We established a robust 3D printing methodology for generating micropillar array structures with multiscale hierarchical features using nanoparticles; the power of this method is that multi length-scale features can be tuned. This methodology can be applied to fields where electrode structural considerations are important for performance.

Our fabrication method enabled comparison studies to be performed over a large library of electrodes to identify the bottlenecks currently limiting biophotocatalysis. We demonstrated that although macroporous electrodes offered large EASA for high biocatalyst loading, light and electrolyte penetration was limited through the structure. The micropillar electrode design overcame this issue, and the addition of submicrometre roughness to the surfaces boosted the EASA, cell loadings and light collection. Applying the lessons from this study, future electrode design within the field of photoelectrochemistry should prioritize light flux considerations before introducing highly structured architectures to boost electron flux capacity.

The photocurrent outputs (up to  $245\mu\text{A cm}^{-2}$  for mediated electron transfer, and up to  $1.93\mu\text{A cm}^{-2}$  for direct electron transfer) demonstrated here are a milestone in biophotocatalysis. They bring us one order of magnitude closer to the photocurrents needed for living photosynthetic cells to be competitive in bio-energy generation. For example, when this bio-anode is paired with an appropriate cathode to result in a typical voltage difference (0.213 V), power densities of  $541\text{ mW m}^{-2}$  can be estimated; this already compares favourably with biofuel generation ( $<403\text{ mW m}^{-2}$ )<sup>8</sup>. Lessons from this study will guide the development of future high-performing bio-electrode structures; however, advancements to electron mediation strategies (to replace DCBQ, which exerts cytotoxicity and is unstable) will be important for long-term high performance<sup>34</sup>. This study demonstrates the power of 3D printing in 3D electrode design and opens new directions for understanding and enhancing the bio-electrode interface.

## Online content

Any methods, additional references, Nature Research reporting summaries, source data, extended data, supplementary information, acknowledgements, peer review information; details of author contributions and competing interests; and statements of data and code availability are available at <https://doi.org/10.1038/s41563-022-01205-5>.

Received: 8 July 2021; Accepted: 18 January 2022;  
Published online: 7 March 2022

## References

- Kornienko, N., Zhang, J. Z., Sakimoto, K. K., Yang, P. D. & Reisner, E. Interfacing nature's catalytic machinery with synthetic materials for semi-artificial photosynthesis. *Nat. Nanotechnol.* **13**, 890–899 (2018).
- Zhang, J. Z. & Reisner, E. Advancing photosystem II photoelectrochemistry for semi-artificial photosynthesis. *Nat. Rev. Chem.* **4**, 6–21 (2020).
- King, P. W. Semi-synthetic strategy. *Nat. Energy* **3**, 921–922 (2018).
- Léger, C. & Bertrand, P. Direct electrochemistry of redox enzymes as a tool for mechanistic studies. *Chem. Rev.* **108**, 2379–2438 (2008).
- Saar, K. L. et al. Enhancing power density of biophotovoltaics by decoupling storage and power delivery. *Nat. Energy* **3**, 75–81 (2018).
- Wey, L. T. et al. The development of biophotovoltaic systems for power generation and biological analysis. *ChemElectroChem* **6**, 5375–5386 (2019).
- Zhang, J. Z. et al. Photoelectrochemistry of photosystem II in vitro vs in vivo. *J. Am. Chem. Soc.* **140**, 6–9 (2018).
- McCormick, A. J. et al. Biophotovoltaics: oxygenic photosynthetic organisms in the world of bioelectrochemical systems. *Energy Environ. Sci.* **8**, 1092–1109 (2015).
- Bradley, R. W., Bombelli, P., Lea-Smith, D. J. & Howe, C. J. Terminal oxidase mutants of the cyanobacterium *Synechocystis* sp. PCC 6803 show increased electrogenic activity in biological photo-voltaic systems. *Phys. Chem. Chem. Phys.* **15**, 13611–13618 (2013).
- Sekar, N., Jain, R., Yan, Y. & Ramasamy, R. P. Enhanced photo-bioelectrochemical energy conversion by genetically engineered cyanobacteria. *Biotechnol. Bioeng.* **113**, 675–679 (2016).
- Liu, C., Dasgupta, N. P. & Yang, P. Semiconductor nanowires for artificial photosynthesis. *Chem. Mater.* **26**, 415–422 (2014).
- Mersch, D. et al. Wiring of photosystem II to hydrogenase for photoelectrochemical water splitting. *J. Am. Chem. Soc.* **137**, 8541–8549 (2015).
- Wijnhoven, J. E. & Vos, W. L. Preparation of photonic crystals made of air spheres in titania. *Science* **281**, 802–804 (1998).
- Liu, Y. et al. Macroporous indium tin oxide electrode layers as conducting substrates for immobilization of bulky electroactive guests. *Electrochim. Acta* **140**, 108–115 (2014).
- Riedel, M. & Lisdat, F. Integration of enzymes in polyaniline-sensitized 3D inverse opal  $\text{TiO}_2$  architectures for light-driven biocatalysis and light-to-current conversion. *ACS Appl. Mater. Interfaces* **10**, 267–277 (2018).
- Xia, L. et al. Zinc oxide inverse opal electrodes modified by glucose oxidase for electrochemical and photoelectrochemical biosensor. *Biosens. Bioelectron.* **59**, 350–357 (2014).
- Arsenault, E., Soheilnia, N. & Ozin, G. A. Periodic macroporous nanocrystalline antimony-doped tin oxide electrode. *ACS Nano* **5**, 2984–2988 (2011).
- Wenzel, T., Härtter, D., Bombelli, P., Howe, C. J. & Steiner, U. Porous translucent electrodes enhance current generation from photosynthetic biofilms. *Nat. Commun.* **9**, 1299 (2018).
- Fang, X., Kalathil, S., Divitini, G., Wang, Q. & Reisner, E. A three-dimensional hybrid electrode with electroactive microbes for efficient electrogenesis and chemical synthesis. *Proc. Natl Acad. Sci. USA* **117**, 5074–5080 (2020).
- Sturmberg, B. C. P. et al. Modal analysis of enhanced absorption in silicon nanowire arrays. *Opt. Express* **19**, A1067–A1081 (2011).
- Ali, M. Nanostructured photoelectrochemical solar cell for nitrogen reduction using plasmon-enhanced black silicon. *Nat. Commun.* **7**, 11335 (2016).
- Wang, K., Chang, Y.-H., Zhang, C. & Wang, B. Conductive-on-demand: tailorable polyimide/carbon nanotube nanocomposite thin film by dual-material aerosol jet printing. *Carbon* **98**, 397–403 (2016).
- Saleh, M. S., Li, J., Park, J. & Panat, R. 3D printed hierarchically-porous microlattice electrode materials for exceptionally high specific capacity and areal capacity lithium ion batteries. *Addit. Manuf.* **23**, 70–78 (2018).
- Saleh, M. S., Hu, C. & Panat, R. Three-dimensional microarchitected materials and devices using nanoparticle assembly by pointwise spatial printing. *Sci. Adv.* **3**, e1601986 (2017).
- Čatić, N. et al. Aerosol-jet printing facilitates the rapid prototyping of microfluidic devices with versatile geometries and precise channel functionalization. *Appl. Mater. Today* **19**, 100618 (2020).
- Jabari, E. & Toyserkani, E. Micro-scale aerosol-jet printing of graphene interconnects. *Carbon* **91**, 321–329 (2015).
- Sukeshini, A. M. et al. Aerosol jet printing and microstructure of SOFC electrolyte and cathode layers. *ECS Trans.* **35**, 2151 (2011).
- Kalio, A. et al. Development of lead-free silver ink for front contact metallization. *Sol. Energy Mater. Sol. Cells* **106**, 51–54 (2012).



29. Lu, S. et al. Flexible, print-in-place 1D–2D thin-film transistors using aerosol jet printing. *ACS Nano* **13**, 11263–11272 (2019).
30. Hong, K. et al. Aerosol jet printed, sub-2 V complementary circuits constructed from P- and N-type electrolyte gated transistors. *Adv. Mater.* **26**, 7032–7037 (2014).
31. Lin, J.-T. et al. A high-efficiency HIT solar cell with pillar texturing. *IEEE J. Photovolt.* **8**, 669–675 (2018).
32. Saini, D. K., Pabbi, S. & Shukla, P. Cyanobacterial pigments: perspectives and biotechnological approaches. *Food Chem. Toxicol.* **120**, 616–624 (2018).
33. Wey, L. T. et al. A biophotoredochemical approach to unravelling the role of cyanobacterial cell structures in exoelectrogenesis. *Electrochim. Acta* **395**, 139214 (2021).
34. Clifford, E. R. et al. Phenazines as model low-midpoint potential electron shuttles for photosynthetic bioelectrochemical systems. *Chem. Sci.* **12**, 3328–3338 (2021).
35. Torimura, M., Miki, A., Wadano, A., Kano, K. & Ikeda, T. Electrochemical investigation of cyanobacteria *Synechococcus* sp. PCC7942-catalyzed photoreduction of exogenous quinones and photoelectrochemical oxidation of water. *J. Electroanal. Chem.* **496**, 21–28 (2001).
36. Reggente, M., Politi, S., Antonucci, A., Tamburri, E. & Boghossian, A. A. Design of optimized PEDOT-based electrodes for enhancing performance of living photovoltaics based on phototropic bacteria. *Adv. Mater. Technol.* **5**, 1900931 (2020).
37. Cereda, A. et al. A bioelectrochemical approach to characterize extracellular electron transfer by *Synechocystis* sp. PCC6803. *PLoS ONE* **9**, e91484 (2014).
38. Zeng, Y. et al. Photoactive conjugated polymer-based hybrid biosystems for enhancing cyanobacterial photosynthesis and regulating redox state of protein. *Adv. Funct. Mater.* **31**, 2007814 (2021).

**Publisher's note** Springer Nature remains neutral with regard to jurisdictional claims in published maps and institutional affiliations.

© The Author(s), under exclusive licence to Springer Nature Limited 2022



## Methods

**Electrode fabrication.** *IO-ITO electrodes.* The microporous electrodes (10 µm pores, ~3 µm channels, 50 µm thickness) were prepared using templated synthesis via an infiltration approach adopted from a previous study<sup>7</sup>, with small adjustments. Briefly, cleaned fluorine-doped tin oxide (FTO)-coated glass (sheet resistance in 8 Ω cm<sup>-2</sup>, Sigma-Aldrich) were applied with a mould in the form of a hole, with a geometric surface area of 0.0625 cm<sup>2</sup> (prepared from electrical tape 25 mm thick). The FTO-coated glass with the attached mould was O<sub>2</sub>-treated (UV/Ozone Procleaner, Bioforce Nanosciences) for 15 min. Polystyrene beads (10 µm diameter, 2.54% w/v suspension in water, Alfar Asaer) were spun down via centrifugation (12,300g, 5 min). The polystyrene bead sediments were resuspended with supernatant using one-quarter of the original supernatant. Aliquots of the polystyrene bead suspension (30 µl) were spread inside the mould of the FTO-coated slides. To allow for uniform sedimentation, the polystyrene beads were slowly dried by evaporation over 3 h, followed by 10 min sintering at 80 °C. ITO nanoparticles (80 mg, <50 nm diameter, Sigma-Aldrich) were combined with a mixture of MeOH (252 µl) and deionized water (48 µl). The ITO suspension was ultrasonicated for 5 h at 50 °C. The ITO suspension (6.8 µl) was dropcast onto the polystyrene bead template and allowed to infiltrate slowly over approximately 1 h. The electrodes were annealed at 500 °C for 20 min (ramp rate, 1 °C min<sup>-1</sup>; carbolite furnace).

*SP-ITO and BP-ITO electrodes.* All micropillar structures were fabricated with an aerosol jet printer (AJ200, Optomec) using an ITO precursor (36% w/v) prepared from a solvent mixture of water and MeOH. The ratio of water to MeOH was systematically changed from 6:1 to 1:6 to investigate the effect of solvent on pillar geometry formation. This ratio range is compatible with the ultrasonic atomizer with precursor viscosity no higher than 5 cP. The ITO ink precursor (2 ml) was ultrasonicated at 50 °C for 3 h before use. The ITO precursor was then transferred to the ultrasonic atomizer, which was maintained at a constant temperature of 14 °C using a water jacket.

The aerosol jet printer was situated inside a glovebox (MBRAUN) in an ultra-clean and highly purified gas environment with O<sub>2</sub> and H<sub>2</sub>O concentrations <1 ppm. Dry N<sub>2</sub> (HPCL grade, 99.998%) was used as the carrier gas of the ITO stream, which was set between 0 and 50 standard cubic centimetres minute (sccm). The focused sheath gas was set between 0 sccm and 200 sccm and the atomized current was maintained at 0.4 mA. The flow rates of the gasses were measured at their inlets of the printer. A 7.5 mm long nozzle with a diameter of 150 µm was used for printing. The electrodes were annealed at 500 °C for 20 min (ramp rate, 1 °C min<sup>-1</sup>; carbolite furnace).

More information on the operational mechanisms of the aerosol jet spray printing process can be found in the Supplementary Information.

**Electrode characterization.** *SEM and EDX.* SEM was conducted with a Tescan Mira3 FEG-SEM operated at an acceleration voltage of 5 kV. All the imaged samples were sputtered with a 10 nm layer of Pt to prevent charging. EDX was performed on a Zeiss Auriga using 20 kV electron acceleration voltage at a working distance of 5 mm.

*Transmission and reflection measurements.* The electrode structures (IO-ITO, SP-ITO and BP-ITO) were sealed by a 3D-printed circular silicon mould (diameter, 1 cm; area, 0.75 cm<sup>2</sup>; height, 3 cm), covered by thin glass (thickness, 0.13 mm; Sigma-Aldrich). This set-up was necessary to avoid the drying out of the pillar arrays, which could lead to collapsed pillars due to capillary load (Supplementary Fig. 12). A light source (Xenon lamp, Ocean Optics HPX-2000) was coupled in an optical fibre (Thorlabs FC-UV100-2-SR) to illuminate the sample placed in front (transmission) or at the back (reflection) of an integrated sphere (Labsphere). The scattered light was collected into an optical fibre, which was connected to a spectrometer (Avantes HS2048) for the measurements (Supplementary Fig. 4). For the transmission measurements, the illuminated light signal was normalized to the intensity (equivalent to 1 mW cm<sup>-2</sup> at wavelength 680 nm) without samples. For the reflection measurements, the light signal was normalized according to the coating of the integrated sphere. FTO-glass (thickness, 3 mm; Sigma-Aldrich) and cover-slip glass (thickness, 0.13 mm; Sigma-Aldrich) were measured as the reference for both reflection and transmission tests. An unpolarized light was used with integration time of 2 s.

*Electroactive surface area characterization.* The EASA was calculated from the capacitance of the electrodes, which was measured using cyclic voltammetry at different scan rates using the ITO electrodes as the working electrode, Pt mesh as the counter electrode and Ag/AgCl (KCl saturated) as the reference electrode. The electrolyte used was 1,1'-ferrocenedimethanol (1 mM in 1-butyl-3-methylimidazolium hexafluorophosphate). The capacitance was analysed using equation (1) below:

$$\frac{i_a - i_c}{2} = C\nu \quad (1)$$

where  $C$  is the capacitance (F),  $i_a$  is the anodic current (A) measured at 0.3 V versus standard hydrogen electrode (SHE),  $i_c$  is the equivalent cathodic current (A) measured at 0.3 V versus SHE and  $\nu$  is the scan rate (V s<sup>-1</sup>). An aerosol jet-sprayed flat ITO surface (0.0625 cm<sup>2</sup>) was used as the planar surface reference.

Cyclic voltammetry curves at different scan rates were carried out with the intention of exploiting the Randles–Ševčík equation to estimate the EASA using the peak currents of the 1,1'-ferrocenedimethanol. However, at high scan rates, quasi-reversible peaks were observed, which precluded the use of this analysis method (Supplementary Note 4).

**Cell-loaded electrodes characterization.** *Cell culturing.* *Synechocystis* sp. strain PCC 6803 (Howe laboratory wild-type strain) was grown photoautotrophically at 30 °C with a continuous white light intensity of 50 µE m<sup>-2</sup> s<sup>-1</sup> in BG11 medium supplemented with 10 mM NaHCO<sub>3</sub> (ref. <sup>39</sup>). Glycerol stocks were streaked onto agar plates (with solid medium containing 1.5% agar). Individual colonies were picked to inoculate liquid cultures, which were air-bubbled and shaken at 120 r.p.m. Growth of liquid cultures was monitored by attenuation (OD<sub>750</sub>) with Chl *a* concentration determined by absorbances ( $A$ ) at 680 and 750 nm:  $(A_{680} - A_{750}) \times 10.814$  (ref. <sup>40</sup>).

The early stationary phase planktonic cultures (OD<sub>750</sub> = 1) were centrifuged for 10 min at 5,000g and resuspended in fresh BG11 to a concentration of 150 nmol Chl *a* ml<sup>-1</sup> before photoelectrochemistry experiments.

*Cell loading on electrodes.* A 3D-printed silicon circular mould (area = 0.75 cm<sup>2</sup>) with height of 3 cm was used to surround the printed electrode structure on the FTO-coated glass in a water-tight manner. Concentrated *Synechocystis* suspensions (30 µl, 150 nmol Chl *a* mL<sup>-1</sup>) were pipetted into the silicon mould and allowed to incubate in the dark for 12 h. The mould functioned to decrease the rate of cell settling to the bottom of the electrodes. After 12 h, the cell-loaded electrodes were carefully submerged with fresh BG11 to wash off loosely bound cells.

The cell loadings on the electrodes were determined using a previously reported method<sup>7</sup>. The concentrations of Chl *a* loaded onto electrodes were typically measured immediately after photoelectrochemical or light transmission/reflection experiments. The cell-loaded ITO electrodes were scraped with a pipette tip from the substrate glass and into a microcentrifuge tube containing 500 µl MeOH. To avoid photodegradation of Chl *a*, the vial was covered with aluminium foil, then placed in an ultrasonic bath cooled to 0 °C and sonicated for 30 min to extract all Chl *a*. The suspension was further centrifuged at 13,000g for 3 min and the supernatant was analysed by UV-visible spectrometry using the absorbance 665 nm and 750 nm:  $\left( \frac{A_{665} - A_{750}}{79.95 (\text{Chl } a \text{ mg})^{-1} \text{ cm}^{-1}} \right)$

All UV-visible spectrophotometry measurements were made on a Varian Cary 50 Bio.

*Confocal fluorescence microscopy.* A Leica TCS SP8 confocal microscope with a ×10 magnification objective was used to image cell attachment to the electrode structures following cell loading. A 633 nm laser (HeNe) was employed to excite biological cells, and the fluorescence was collected by a low-noise hybrid detector in the range 650–750 nm. Z-stack images were acquired via sequential scanning downwards from the electrode surface to the FTO-glass substrate, to the depth of 50 µm (Z-depth 0.5 µm).

*Photoelectrochemistry.* Photoelectrochemical experiments were carried out using an Ivium CompactStat potentiostat. A Pt mesh counter electrode and an Ag/AgCl (saturated KCl) reference electrode were used in combination with the cell-loaded ITO working electrodes. The water-jacketed electrochemical cell was maintained at 25 °C and BG11 medium (pH 8.5) was used as electrolyte. A red light-emitting diode (LED) light source ( $\lambda = 680$  nm; THORLABS) at intensity of 1 mW cm<sup>-2</sup> (which is equivalent to 56.8 µmol photons m<sup>-2</sup> s<sup>-1</sup>) was employed in the comparison studies. Chronoamperometry was carried out under light/dark cycles of 300 s on and 300 s off with an applied potential of 0.3 V (versus SHE) used in the absence of an exogenous electron mediator, and 0.5 V (versus SHE) used in the presence of DCBQ (1 mM). Where stated, a white LED light source (THORLABS, SM2F32-A) was also employed, and light responses were tested at intensities that varied from 1 mW cm<sup>-2</sup> to 5 mW cm<sup>-2</sup>. All chronoamperometry experiments were given 90 s of equilibrium period in the dark before initial light irradiation. It should be noted that in the presence of DCBQ, the mediated photocurrents drop rapidly, possibly due to diffusional limitations of the mediator in the unstirred electrolyte and partial cytotoxicity effects<sup>41,42</sup>. As such, only the initial (first light cycle) mediated photocurrents were analysed.

*EQE calculations.* EQE is calculated on the basis of the percentage of incoming photons converted to electrons at a certain bias potential and can be calculated by the equation listed below:

$$\text{EQE}(\%) = \frac{123.98/(\mu\text{A cm}^{-2})}{\lambda(\text{nm})[I(\text{mW cm}^{-2})]}$$

*Statistical analysis.* Single-tailed analysis of variance was performed using the Data Analysis ToolPak in Microsoft Excel to calculate  $P$  values when comparing experimental data, using a significance threshold of  $P \leq 0.05$ . Correlation analysis was performed in the R environment (v.4.0.4)<sup>43</sup>. Quantitative data of electrodes were expressed as means ( $n = 12$ ). Microroughness was expressed as a binary

integer (0 = SP-ITO, 1 = BP-ITO). Pairwise Spearman's rank correlations and *P* values were calculated and visualized as a correlation matrix using the 'corrplot' package<sup>44</sup>. See Supplementary Note 3 for a tutorial explanation of this analysis. The data and code used in the correlation analysis are available via the Apollo repository (<https://doi.org/10.17863/CAM.80096>) or on Github (<https://github.com/JLawrence96/MicropillarArrayElectrodes>).

### Data availability

All data used in this paper are available via the Apollo repository (<https://doi.org/10.17863/CAM.80096>) or on GitHub (<https://github.com/JLawrence96/MicropillarArrayElectrodes>).

### Code availability

All code used in this paper are available via the Apollo repository (<https://doi.org/10.17863/CAM.80096>) or on GitHub (<https://github.com/JLawrence96/MicropillarArrayElectrodes>).

### References

39. Stanier, R. Y., Kunisawa, R., Mandel, M. & Cohen-Bazire, G. Purification and properties of unicellular blue-green algae (order Chroococcales). *Bacteriol. Rev.* **35**, 171–205 (1971).
40. Lea-Smith, D. J. et al. Thylakoid terminal oxidases are essential for the cyanobacterium *Synechocystis* sp. PCC 6803 to survive rapidly changing light intensities. *Plant Physiol.* **162**, 484–495 (2013).
41. Yang, C., Zhou, E., Miyanishi, S., Hashimoto, K. & Tajima, K. Preparation of active layers in polymer solar cells by aerosol jet printing. *ACS Appl. Mater. Interfaces* **3**, 4053–4058 (2011).
42. Fang, X. et al. Structure–activity relationships of hierarchical three-dimensional electrodes with photosystem II for semiartificial photosynthesis. *Nano Lett.* **19**, 1844–1850 (2019).
43. R Core Team *R: A Language and Environment for Statistical Computing* (R Foundation for Statistical Computing, 2013).
44. Wei, T. & Simko, V. corrplot: visualization of a correlation matrix. R package version 0.84 <https://github.com/taiyun/corrplot> (2017).

### Acknowledgements

This work was supported by the Biotechnology and Biological Sciences Research Council (BB/M011194/1 to J.M.L., BB/R011923/1 to J.Z. and X.C.), the Cambridge Trust (L.T.W.) and the Isaac Newton Trust (SCHERTEL SNSF3 to L.S.). S.K.-N. is grateful for support from a European Research Council (ERC) Starting Grant (ERC-2014-STG-639526, NANOGEN). S.K.-N. and Q.J. acknowledge support from the EPSRC Centre of Advanced Materials for Integrated Energy Systems (CAM-IES) (grant EP/P007767/1). We thank H. Lloyd-Laney and E. Kitson for helpful discussions in statistical analysis. We thank N. Plumeré and H. Li for helpful discussions in electrochemistry. We thank P. J. Bártolo and F. Liu for helpful discussions in 3D bioprinting.

### Author contributions

J.Z.Z. and X.C. conceived the project and wrote the manuscript. X.C. was the lead experimenter, interpreted the data and produced Figs. 1–4. J.M.L. helped with the preparation of the manuscript, performed and interpreted the statistical analysis, and produced Fig. 5b. L.T.W. provided biological samples and expertise. L.S. helped to design and carry out and interpret the light transmission/reflection/absorption experiments. Q.J. helped to establish the initial protocol for aerosol jet printing pillars. S.V. helped guide the light experiments. C.J.H. contributed biological expertise and samples. S.K.-N. helped to guide the initial printing experiments. All contributed comments to the manuscript.

### Competing interests

The authors declare no competing interests.

### Additional information

**Supplementary information** The online version contains supplementary material available at <https://doi.org/10.1038/s41563-022-01205-5>.

**Correspondence and requests for materials** should be addressed to Jenny Z. Zhang.

**Peer review information** *Nature Materials* thanks Lars Jeuken and the other, anonymous, reviewer(s) for their contribution to the peer review of this work.

**Reprints and permissions information** is available at [www.nature.com/reprints](http://www.nature.com/reprints).